Journal of Alloys and Compounds 509 (2011) 6955–6961

Contents lists available at ScienceDirect

Journal of Alloys and Compounds

journal homepage: www.elsevier.com/locate/jallcom

# Electrochemical performance of microwave synthesized $Nd_{1.8}Ce_{0.2}CuO_{4\pm\delta}$ cathode for intermediate temperature solid oxide fuel cell applications

A.P. Khandale, S.S. Bhoga*

*Department of Physics, RTM Nagpur University, Amravati Road, Nagpur 440 033, Maharashtra, India*

ARTICLE INFO

*Article history:*
Received 16 February 2011
Received in revised form 27 March 2011
Accepted 2 April 2011
Available online 12 April 2011

*Keywords:*
Electrochemical impedance spectroscopy (EIS)
Area-specific resistance (ASR)
Cathode
Mixed ionic–electronic conductor (MIEC)
dc electrical conductivity

ABSTRACT

The microwave combustion of reagents followed by microwave sintering resulted in superfine crystalline $Nd_{1.8}Ce_{0.2}CuO_{4\pm\delta}$ solid solution. The $Nd_{1.8}Ce_{0.2}CuO_{4\pm\delta}$ crystal lattice volume increases with the reduction of crystallite size. Increase in sintering temperature increases crystallite size and sintered density. A good interfacial contact between $Ce_{0.9}Gd_{0.1}O_2$ electrolyte and $Nd_{1.8}Ce_{0.2}CuO_{4\pm\delta}$ cathode forms to yield symmetric cells for electrochemical studies. The electrochemical impedance data obtained at various temperatures simulated using electrical equivalent circuit. The low-frequency response well fitted to Gerischer element. The sintering temperature 900 °C during the cathode preparation is optimized on the basis of least area-specific-resistance (ASR) = 1.19 Ω cm$^{-2}$ at 700 °C.



## 1. Introduction

Mixed ionic–electronic conductors (MIECs) have gained considerable attention as a potential cathode for intermediate temperature solid oxide fuel cells (IT-SOFCs) due to their interesting transport, mechanical and catalytic properties [1–3]. The advantage of using MIEC cathode in IT-SOFC has resulted in enhanced electrochemically active area, also, lowered operating temperature from 1000 °C to 500–700 °C [4].

Many mixed oxides of the type $A_2BO_4$ ($A$ = rare earth, alkaline earth; $B$ = transition metal) crystallized with the tetragonal $K_2NiF_4$ – type structure (space group $I4/mmm$) have received renewed interest. Such $A_2BO_4$ type oxides have been of considerable interest due to adequate oxygen conduction, strong electrocatalytic activity towards the oxygen reduction and the thermal expansion coefficient (TEC) comparable with those of the conventional electrolytes [1,5].

Significant mixed ionic and electronic conductivities with appreciable electrocatalytic activity have been found in $Ln_2NiO_4$ and $Ln_2CuO_4$ systems having $K_2NiF_4$ – type structure [6–10]. In addition to these, the thermochemical stability of $K_2NiF_4$ – type manganites, ferrites, cuperates and nickelates has been reported higher than those of the corresponding perovskite – type oxides [10]. The Co- and Fe-containing $K_2NiF_4$ compounds have been studied extensively in near recent past [11,12]. Although the total conductivity and the TEC of $La_{2-x}Sr_xCuO_{4\pm\delta}$ materials have been fairly satisfactory, they exhibit rather high area specific resistance (ASR) [4,10]. On the other hand, the ASR of $Nd_{1.7}Sr_{0.3}CuO_4$ cathode on samarium-doped ceria (SDC) electrolyte has been found satisfactory [10]. Soorie and Skinner have reported the preliminary study on the $Nd_{2-x}Ce_xCuO_{4\pm\delta}$ ($0 \le x \le 0.2$) with both the GDC ($Ce_{0.9}Gd_{0.1}O_{1.95}$) and the LSGM ($La_{0.9}Sr_{0.1}Ga_{0.8}Mg_{0.2}O_{3\pm\delta}$) electrolytes [13]. The solid solubility of Ce in $Nd_2CuO_4$ has been established up to $x = 0.2$ [13]. Preliminary studies on mechanochemically derived $Nd_{1.8}Ce_{0.2}CuO_{4\pm\delta}$ solid solution showed promising results [14]. In this regard there is ample scope to prepare these materials following different techniques to obtain superfine/nanocrystalline powder so as to improve further the electrical as well as the catalytic activity.

In the light of above facts the present study was aimed at preparing $Nd_{1.8}Ce_{0.2}CuO_{4\pm\delta}$ using microwave combustion technique followed by microwave sintering to see the effect of preparative technique on electrical and electrochemical properties. The prepared samples were characterized by X-ray powder diffraction (XRD), scanning electron microscopy (SEM), dc electrical conductivity. The electrochemical performance using electrochemical impedance spectroscopy (EIS) was carried out on the symmetric cells with configuration given below.

$Nd_{1.8}Ce_{0.2}CuO_{4\pm\delta}$/GDC/$Nd_{1.8}Ce_{0.2}CuO_{4\pm\delta}$

* Corresponding author. Fax: +91 7122500736.
*E-mail address:* msrl.physics1@gmail.com (S.S. Bhoga).

0925-8388/$ – see front matter © 2011 Elsevier B.V. All rights reserved.
doi:10.1016/j.jallcom.2011.04.012

The improved electrochemical performance is discussed in the light of microstructural results.

## 2. Experimental

The reagents acetates of cerium, neodymium and copper, purity >99.9%, used were procured from Aldrich Chemicals, USA. All the well-dried reagents in requisite stoichiometric ratio were taken and dissolved in the double distilled deionised water, separately. Later, all the solutions were mixed together in a single corning flask, stirred to homogenize solution and then charred with the help of microwave oven at an output power of 800 W. The residue thus obtained was ground to fine powder. Pellets of diameter and thickness 9 and 1–2 mm, respectively, were obtained by uniaxially compressing ground powder at 3 tons $cm^{-2}$ pressure with the help of Specac (UK) stainless steel die-punch and hydraulic press. The resulting pellets were finally sintered separately at 800, 900 and 1000 °C for 4 h using microwave furnace (CEM, USA). Samples sintered at 800, 900 and 1000 °C are designated as NCCO-8, NCCO-9 and NCCO-10, respectively.

All the prepared samples were characterized using X-ray powder diffraction (XRD), and scanning electron microscopy (SEM). The density of the sintered pellets was measured following Archimedes principle with the help of Mettler XS105 dual range monopan balance with density kit attachment and built in density measurement software. Microhardness was measured by the Vickers indentation technique (HMV-2 microhardness tester, Shimadzu, Japan).

The slurry/ink of $Nd_{1.8}Ce_{0.2}CuO_{4\pm\delta}$ cathode for electrochemical studies was obtained as follows. 1 g of $Nd_{1.8}Ce_{0.2}CuO_{4\pm\delta}$ powder sintered at 900 °C (NCCO-9) was mixed with 3 wt% polyvinyl buteral binder, sodium free corn oil and ethyl methyl ketone. The mixture was then ball-milled using Pulverisette-6 (Fritsch, Germany) for 2 h with 300 revolutions per minute (rpm). The two hundred-zirconia balls of 5 mm diameter and 80 ml bowl of tungsten carbide were used. Similar procedure was followed to obtain the ink of $Nd_{1.8}Ce_{0.2}CuO_{4\pm\delta}$ sintered at 800 and 1000 °C (NCCO-8 and NCCO-10). The GDC (10 mole% gadolinium doped ceria) nano-powder (Aldrich, USA) was pressed in a similar manner as described above to obtain pellets of diameter 9 mm and thickness 1–2 mm. They were then sintered at 1400 °C for 6 h. The sintered density about 96% was achieved. Both the flat surfaces of the GDC pellet were then roughened with # 60 grid paper and cleaned with acetone. The slurry/ink of each cathode material was then coated on both the flat surfaces of GDC electrolyte pellet using spin coater at 3000 rpm for 60 s to obtain the symmetric cells with configuration given below,

$$Nd_{1.8}Ce_{0.2}CuO_{4\pm\delta}/GDC/Nd_{1.8}Ce_{0.2}CuO_{4\pm\delta}$$

The symmetric cells were initially baked at 400 °C for 1 h so as to burn out the organic binders and then finally sintered at 700 °C for 2 h in microwave furnace. Hereafter, symmetric cells prepared by using ink of $Nd_{1.8}Ce_{0.2}CuO_{4\pm\delta}$ sintered at 800, 900 and 1000 °C will be referred to as Cell-1, Cell-2 and Cell-3, respectively. The details of dc conductivity on cathode pellet and electrochemical impedance spectroscopy on symmetric cells measurements are described elsewhere [14].

## 3. Results and discussion

### 3.1. X-ray powder diffraction and sintered density

Typical X-ray powder diffraction (XRD) patterns of $Nd_{1.8}Ce_{0.2}CuO_{4\pm\delta}$ sintered at 800, 900 and 1000 °C are shown in Fig. 1(a–c), respectively. In general, all the diffracted lines are broader than usual ones. The broadening of diffracted lines is attributed to the superfine crystalline nature of materials. The obtained XRD data were profile fitted with the help of X'pert Highscore plus software before indexing. Fig. 1(a–c) reveals close matching of characteristic diffracted lines with the JCPDS (joint committee for powder diffraction standard) data (File No. 01-084-2177) corresponding to pure $Nd_2CuO_4$. The absence of line(s) corresponding to either pure reagents or intermediate phases confirmed the formation of single-phase tetragonal $Nd_{1.8}Ce_{0.2}CuO_{4\pm\delta}$ solid solution. A close look at Fig. 1(a–c) reveals increase in sharpness of diffracted lines; i.e. full width of half maxima (FWHM) reduces with increase in sintering temperature. Increased sharpness of diffracted lines (reduced FWHM) implies the improved crystallinity due to increased sintering temperature. These results are in line with the general observation that increased sintering temperature enhances crystallinity in case of poor crystalline materials.

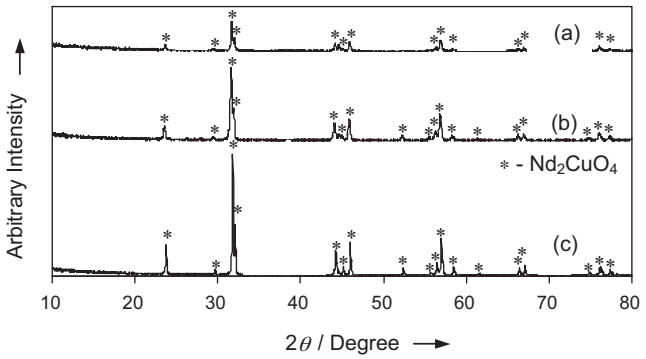


**Fig. 1.** A comparison of X-ray powder diffraction patterns of (a) NCCO-8, (b) NCCO-9 and (c) NCCO-10.

The crystallite size of all the samples under study determined using X'pert Highscore employing formulae given below,

$$C_s = \frac{0.9\lambda}{\beta \cos\theta_B}, \quad (1)$$

where $C_s$, $\lambda$, and $\theta_B$ are crystallite size, X-ray wavelength and Bragg's angle, respectively. Here, $\beta$ was obtained using Eq. (2),

$$\beta^2 = \beta_m^2 - \beta_s^2, \quad (2)$$

where, $\beta_m$ and $\beta_s$ are the measured and the standard FWHM of diffracted line, respectively. The $\beta_s$ was estimated from the XRD pattern obtained by running the experiment on a standard silicon sample supplied by PANalytical, Netherlands. A close scrutiny of Table 1 suggests nanocrystalline nature of all the compositions under study. Furthermore, the crystallite size increases with an increase in sintering temperature. On the other hand, lattice strain decreases with increase in sintering temperature. As expected the sintered density of $Nd_{1.8}Ce_{0.2}CuO_{4\pm\delta}$ (Table 1) enhances with increased sintering temperature. The enhanced sintered density commensurately increases the microhardness of the sample (Table 1). Both these results compliment each other. The increase in sintering temperature facilitates grain growth at the cost of grain-boundary, which in turn increases the sintered density as well as microhardness number.

The lattice cell constants for NCCO-8, NCCO-9 and NCCO-10 were determined using Unit cell, computer software [15] and compared in Table 1. Evidently, the lattice cell volume increases with the reduction in the crystallite size (Table 1). Similar results have been observed in case of strontium doped lanthanum manganite (LSM) [16]. Such lattice expansion has also been demonstrated for ultra-fine hematite crystallite, wherein uniform elastic expansion of lattice took place due to the effect of the action of adjoining surface tension force [17].

**Table 1**
A comparison of lattice cell constants ($c/a$ and $v$), crystallite size ($C_s$), lattice strain ($L_s$), sintered density ($\rho$), and microhardness number (HV) for $Nd_{1.8}Ce_{0.2}CuO_{4\pm\delta}$ sintered at 800, 900 and 1000 °C ($T_s$ – sintering temperature).

| Sample | $T_s$ (°C) | $c/a$ | $v$ (Å$^3$) | $C_s$ (Å) | $L_s$ (%) | $\rho$ (%) | HV no. |
|---|---|---|---|---|---|---|---|
| NCCO-8 | 800 | 3.062 | 189.66 | 670 | 0.23 | 80.18 | 106 |
| NCCO-9 | 900 | 3.066 | 187.52 | 1018 | 0.20 | 82.58 | 117 |
| NCCO-10 | 1000 | 3.064 | 187.54 | 1797 | 0.13 | 88.34 | 215 |

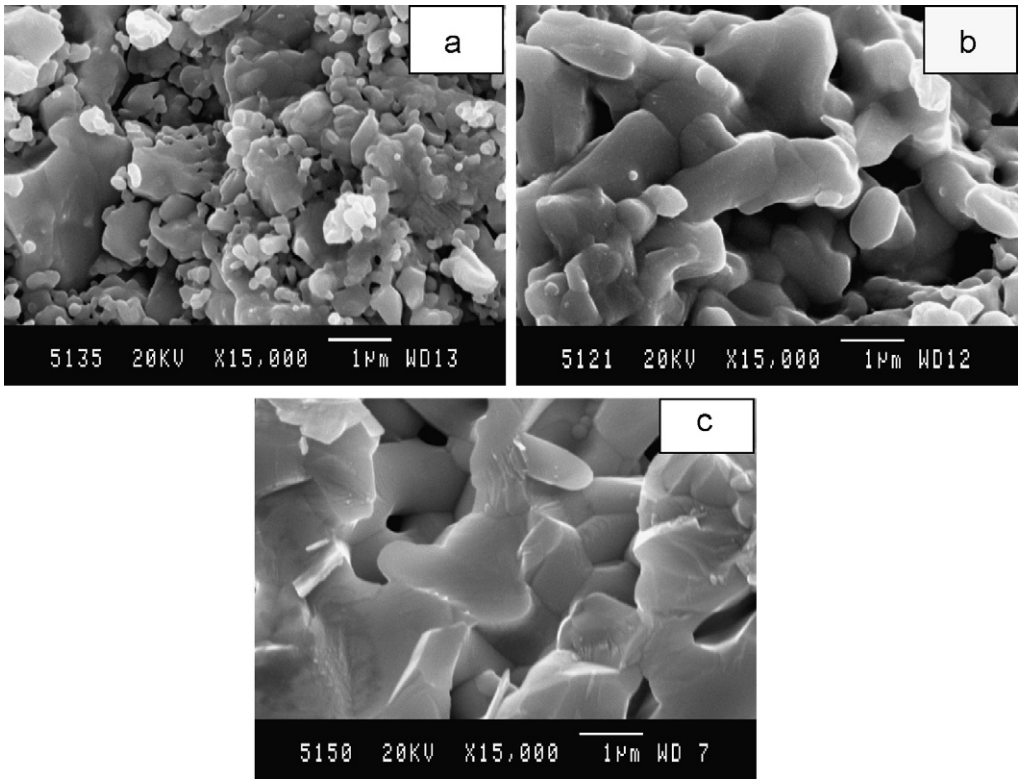


**Fig. 2.** SEM microphotographs of (a) NCCO-8, (b) NCCO-9 and (c) NCCO-10.

### 3.2. Scanning electron microscopy (SEM)

SEM microphotographs of NCCO-8, NCCO-9 and NCCO-10 are depicted in Fig. 2(a–c), respectively. A cursory look at Fig. 2 (a–c) indicated an increased grain size with increase in sintering temperature. This is in line with the general observation i.e., during sintering the grains grow at the cost of neighboring grains and pores. A close scrutiny of Fig. 2(a–c) revealed a large variation in the grain size and shape when microwave combusted powder sintered at relatively lower temperature. On the other hand, with increased sintering temperature uniform grain size and shape is evident (Fig. 2(b and c)). The SEM microphotographs of cathode

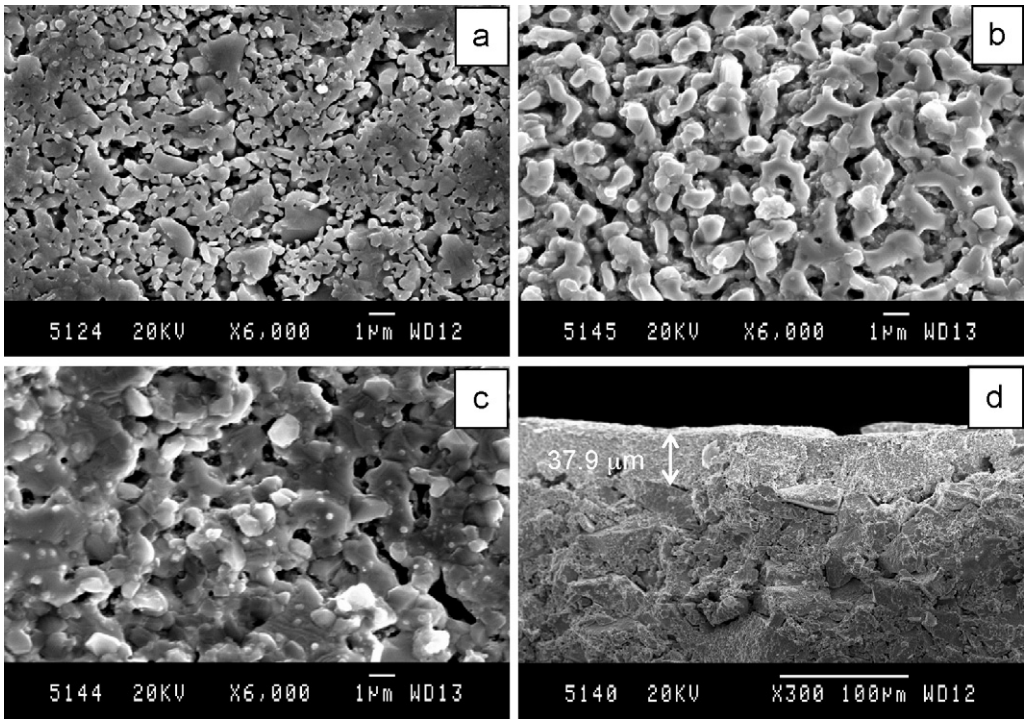


**Fig. 3.** SEM microphotographs of electrode surface of (a) Cell-1, (b) Cell-2 (c) Cell-3 and (d) fractured electrode–electrolyte interface of Cell-2.

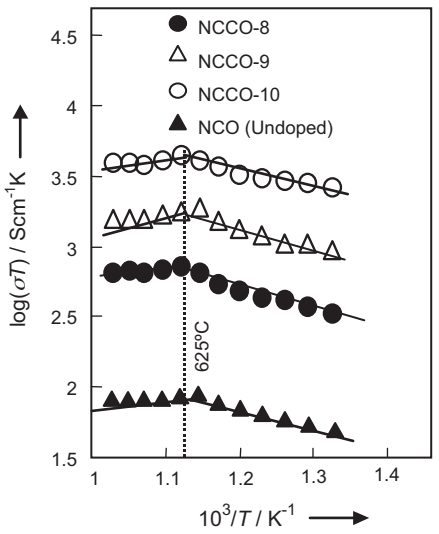


**Fig. 4.** A comparison of temperature dependent dc conductivity of NCO (undoped), NCCO-8, NCCO-9 and NCCO-10.

surface of Cell-1, Cell-2 and Cell-3 along with the fractured surface across interface of Cell-2 are given in Fig. 3(a–d), respectively. As seen, the grains of cathode of Cell-1 (Fig. 3(a)) are non-uniform and have different sizes. Furthermore, grain-to-grain contact is poor. The grains of cathode of Cell-2, however, are uniform and of almost same size that led to uniform distribution of micro-pores (Fig. 3(b)). On the other hand, grain growth due to sintering at high temperature reduced the porosity of cathode layer in case of Cell-3 (Fig. 3(c)). The electrode of thickness ≈37.9 μm forms intimate contact with electrolytes in Cell-2 (Fig. 3(d)). Micro-cracks seen at the interface are due to mechanically fractured cell for SEM study.

### 3.3. dc conductivity

The variation of dc conductivity as a parametric function of temperature for all the samples under study is shown in Fig. 4. In general, the $Nd_{1.8}Ce_{0.2}CuO_{4\pm\delta}$ sintered at 800, 900 and 1000 °C exhibit conductivity maxima at about 625 °C. Spinolo et al. have also observed conductivity maximum in case of $Nd_{2-x}Ce_xCuO_4$ (where $x = 0.15$ and 0.2) [18]. Boehm et al. have also observed similar conductivity maximum in the case of $La_2Ni_{1-x}Cu_xO_{4\pm\delta}$ [19]. Such behaviour is not assigned to semiconductor–metal transition. At temperatures ≤625 °C all samples obey the Arrhenius law,

$$\sigma T = (\sigma T)_0 \ \exp\left(\frac{-E_a}{kT}\right), \tag{3}$$

where $(\sigma T)_0$, $k$, $T$ and $E_a$ are pre-exponential factor, Boltzmann constant, absolute temperature and activation energy, respectively. A close look at Fig. 4 suggests that the conductivity of $Nd_{1.8}Ce_{0.2}CuO_{4\pm\delta}$ is much higher compared to undoped $Nd_2CuO_4$ in the entire temperature range of measurement. Furthermore, the Arrhenius plots (Fig. 4) reveals enhanced dc conductivity with increase in sintering temperature. The enhancement in conductivity with increased temperature is due to increased sintered density (Table 1).

Intrinsically, the electrons and the holes can be produced in $Nd_2CuO_{4\pm\delta}$ lattice by two point defect equilibria given below using Kroger–Vink notations [20]:

$$O_O \Leftrightarrow V_O^{\bullet\bullet} + 2e' + \tfrac{1}{2}O_2 \tag{4}$$

$$\tfrac{1}{2}(O_2) \Leftrightarrow O_i'' + 2h^{\bullet} \tag{5}$$

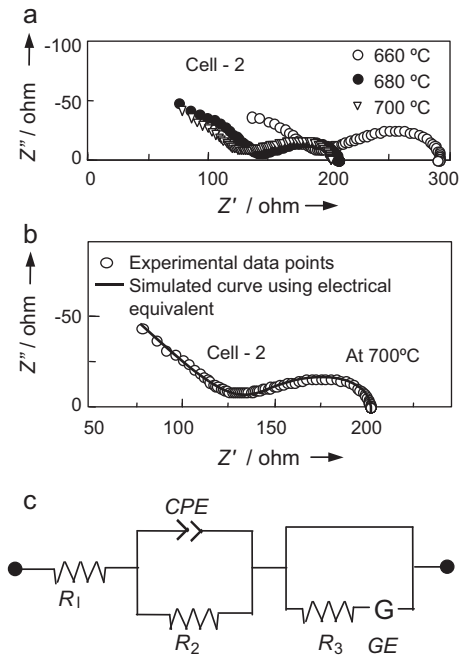


**Fig. 5.** Electrochemical impedance spectra of Cell-2 (a) at various temperatures, (b) simulated and experimental impedance behaviour at 700 °C and (c) electrical equivalent circuit.

coupled with intrinsic ionization:

$$0 \Leftrightarrow e' + h^{\bullet} \tag{6}$$

At intermediate $P_{O_2}$ and temperature (200–625 °C), the doped $Nd_{1.8}Ce_{0.2}CuO_4$ and undoped $Nd_2CuO_4$ are almost oxygen stoichiometric ceramics. In such case carriers are both thermally activated electrons and holes according to Eq. (6). Interestingly, thermoelectric power measurements on $Nd_{1.8}Ce_{0.2}CuO_4$ indicated electrons as majority charge carriers [18]. Consequently, $Nd_2CuO_4$ behaves like semiconductor. At relatively higher temperatures (>625 °C), however, the $Nd_{1.8}Ce_{0.2}CuO_4$ looses some oxygen [18]. According to reaction (5), this process reduces the concentration of hole. Concurrently, correlatively decreases the carrier density (holes) leading to decrease in conductivity. Both these competing phenomena result in the observed maximum of conductivity (Fig. 4). Boehm et al. [19] and Mauvy et al. [21] have discussed in detail the temperature and the oxygen partial pressure dependent behaviour of ASR.

The partial substitution of $Ce^{4+}$ for $Nd^{3+}$ introduces extrinsic defects in $Nd_2CuO_4$ according to quasichemical reaction mentioned below:

$$CuO + 2CeO_2 \rightarrow Cu_{Cu}^{x} + 2Ce_{Nd}^{\bullet} + 4O_o^{x} + 2e' + \tfrac{1}{2}O_2. \tag{7}$$

The electrons, thus created, are associated with the $CuO_2$ planes. The increase in extrinsic mobile electron concentration has been supported by Hall coefficient measurements by Takagi et al. [22]. The extrinsic electrons, thus created, enhance the mobile charge carrier density of $Nd_{1.8}Ce_{0.2}CuO_{4\pm\delta}$ solid solution, which leads to higher conductivity in it compared to undoped $Nd_2CuO_4$ (Fig. 4).

### 3.4. Electrochemical impedance spectroscopy (EIS)

The typical EIS plots for Cell-2 at different temperatures are depicted in Fig. 5(a). Impedance diagrams analyzed using computer programme developed by Scribner advanced software (USA), suggest a clear semicircular arc in the low frequency region. The incomplete semicircular arc in the high frequency region is attributed to the limitation of high frequency (≤1 MHz) of Solartron

1255B FRA. A close look at the Fig. 5 revealed increased *x*-axis intercept of two discernible semicircular arcs with reduced temperature. The first low frequency semicircular arc is not only due to the passage of current through the electrode and across the electrode–electrolyte interface but also due to the complex electrode process. The high frequency incomplete semicircular arc is due to GDC electrolyte. On the other hand, low frequency semicircular arc is due to electrode polarization resulting from reduction of $O_2$ gas reversibly at cathode, and subsequent migration of the $O^{-2}$ across the electrode–electrolyte interface. The increased real axis intercepts of all semicircular arcs with the decrease in temperature suggest increased area-specific resistance (ASR) as well as bulk electrolytic resistance. Almost similar results were obtained for Cell-1 and Cell-3. The electrolytic conductivities for Cell-1, Cell-2 and Cell-3 were obtained at various temperatures from *x*-axis intercept of high frequency semicircle (Fig. 5). The activation energy of GDC evaluated from Arrhenius plots ($\log \sigma T$ vs. $10^3/T$) found nearly same for all cells ($E_a \sim 0.91$ eV) and is in close agreement with the earlier reported value ($E_a = 0.9$ eV) [23]. Thus, the high frequency depressed semicircle is attributed to the migration of $O^{2-}$ through GDC electrolyte. These results are in good agreement with the earlier report [24].

The experimental EIS data along with the simulated response and electrical equivalent circuit model are shown in Fig. 5(b and c), respectively. The EIS response (solid line) simulated using electrical equivalent circuit model (Fig. 5(c)) fitted well with the experimental data (open circles in Fig. 5(b)). The resistance $R_2$ in parallel with *CPE* represents the ion migration through the GDC electrolyte. The *CPE* takes care of depression in high frequency semicircle. The $R_l$ in equivalent circuit represents the lead resistance. It is worth mentioning here that the behaviour of low frequency semicircular arcs (Fig. 5(b)) was better-simulated using Gerischer element (GE) [25] than that using Warburg impedance [26]. The GE in series with the $R_3$ attributed to the reactions of diffusing specie and subsequent migration. The values of simulated circuit elements at various temperatures are displayed in Table 2. As seen the $R_1$, attributed to leads resistance does not change appreciably with change in temperature. On the other hand, the values of $R_2$, and $R_3$ corresponding to electrolytic and electrode resistances increased with reduction in temperature, which is in good agreement with the EIS plots (Fig. 5(a)). Furthermore, the parameters *CPE-T*, *CPE-P* and *GE-T* corresponding to *CPE* and *GE* behaviour increased with reduction in temperature i.e., exhibiting temperature activated behaviour.

Solid electrolyte materials involving conduction via ion-hopping, the immediate microscopic surroundings of different ions would be distinct at a given instant due to either micro-heterogeneity in it [27] or the dynamic relaxation of the positions of atoms surrounding an ion progresses in different amount for unlike ions [28,29]. In both the cases, they are described in terms of distribution of relaxation times arising due to dispersal in activation enthalpies for ion migration. Because, the small differences in activation energies ($E_a$) can lead to large differences in relaxation times $\tau$ according to

$$\tau = \tau_0 \ \exp\left(\frac{E_a}{kT}\right) \tag{8}$$

The physical models have stressed distribution in $\tau$ [30]. Macdonald and Brachman have provided a useful set of integral transform relations between distribution functions and electrical response [31]. van Weperen et al. have developed a theory, based on dipole–dipole interactions, that leads to almost Gaussian distribution of activation energies [32].

Ravaine and Souquet [33], for the first time, have introduced *CPE* element for glassy solid electrolyte (similar to shown in Fig. 5(b)) to account the depressed semicircle in complex impedance plane thereby distribution in $\tau$, of the form

$$Z_{CPE} = A(j\omega)^{-\alpha} \tag{9}$$

here $\alpha$, a measure of depression of semicircular arc in complex impedance plane, lies between 0 and 1. Later Raistrick et al. have applied it to polycrystalline solid electrolyte [34]. Subsequently, *CPE* element has been frequently used in parallel with geometrical capacitance, *C*, and electrolytic bulk resistance, *R* [35,36]. Detailed theoretical description and electrical equivalent circuit for distributed relaxation time (depression in complex impedance plots) have been given in literature [29].

A detailed literature survey revealed scarce use of the Gerischer impedance so far. Makkus et al. [37] have used Gerischer impedance to represent electrode response of an inert gold oxygen electrode in molten carbonate. Atangulov and Murygin [38] derived impedance response theoretically for a gas electrode with slow adsorption and (surface) diffusion. Later, Adler [39] derived GE-type impedance for a porous mixed conducting perovskite oxygen electrode on YSZ.

In case of reversible electrode the current is limited by either slow charge transfer kinetics, or by a process such as adsorption, which effectively controls the concentration of either reactants or products of the charge transfer rate. This leads to a concentration gradient leading to the formation of space charge (double layer) capacitance. This has been viewed as a familiar situation to a single step charge transfer reaction [40].

The rate of single step charge transfer reaction

$$O + ne = R \tag{10}$$

is given by the expression

$$i_F = nF[k_f c_O - k_b c_R] \tag{11}$$

where $i_F$, $k_f$, and $k_b$ are faradic current density, forward and reverse rate constants, respectively. $c_O$ and $c_R$ are the concentrations of the reactants and products at the interface, respectively at time *t*. Such concentration difference in O and R leads to space charge capacitance. The current, in general, is composed of a steady state or dc part determined by the mean dc potential *E* and the mean dc concentrations at the interface, $c_O$ and $c_R$. The ac part, $\Delta i_F$, is determined by the ac perturbing potential $\Delta E$ and the fluctuating concentrations $\Delta c_i$.

A comparison of temperature dependent ASR of Cell-1, Cell-2 and Cell-3 is given in Fig. 6. The transition clearly seen at ≈625 °C, in all the cases, matches with the maximum observed at $T_c \approx 625$ °C in temperature dependent conductivity (Fig. 4). The ASR below and above the $T_c$ obeys Arrhenius law for all cells under study. Furthermore, the Cell-2 exhibits least ASR = 1.19 Ω cm$^{-2}$ at 700 °C amongst all cells under study.

The EIS plots for different values of $P_{O_2}$ around Cell-2 are depicted in Fig. 7(b). In general, there is a considerable variation in the *x*-axis intercept of low frequency semicircular arc with change

**Table 2**
The values of fitted circuit elements corresponding to electrochemical impedance spectra of Cell-2 at various temperatures.

| Sr. # | *T* (°C) | $R_1$ (Ω) | $R_2$ (Ω) | *CPE-T* | *CPE-P* | $R_3$ | *GE-T* | *GE-P* |
|---|---|---|---|---|---|---|---|---|
| 1 | 700 | −14 | 59 | $1.39 \times 10^{-7}$ | 0.54 | 65.5 | 0.0009 | 1.715 |
| 2 | 680 | −16 | 89 | $1.46 \times 10^{-7}$ | 0.62 | 70.3 | 0.044 | 0.31 |
| 3 | 650 | 13 | 104 | $1.55 \times 10^{-7}$ | 0.79 | 114.7 | 0.09 | 0.30 |
| 4 | 580 | 12 | 437 | $2.00 \times 10^{-7}$ | 0.87 | 467.0 | 1.97 | 0.23 |

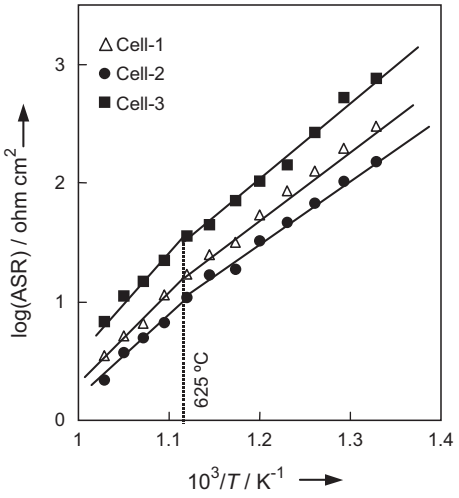


**Fig. 6.** Temperature dependent ASR of Cell-1, Cell-2 and Cell-3.

in $P_{O_2}$. On the other hand, there is very small variation in electrolytic bulk resistance due to change in $P_{O_2}$. The log of polarization resistance exhibited a linear dependence on log $P_{O_2}$ (Fig. 7(b)). Particularly, the ASR varies with the oxygen partial pressure according to the equation,

$$\mathrm{ASR} = \mathrm{ASR}_0(P_{O_2})^{-n} \tag{12}$$

The value of $n$ provides useful information about the type of species involved in the reactions at the electrode [41],

$$n = 1, \quad O_2(g) \Leftrightarrow O_{2,abs} \tag{13}$$

$$n = \frac{1}{2}, \quad O_{2,abs} \Leftrightarrow 2O_{abs} \tag{14}$$

$$n = \frac{1}{4}, \quad O_{abs} + 2e' + V_O^{\bullet\bullet} \Leftrightarrow O_O^x \tag{15}$$

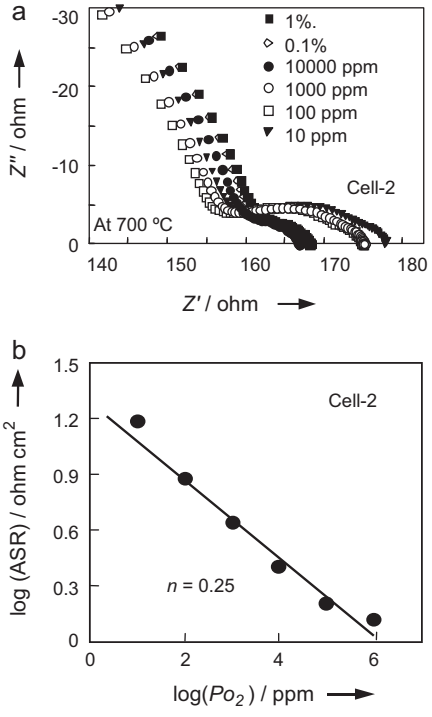


**Fig. 7.** (a) Electrochemical impedance spectra of Cell-2 at various oxygen partial pressures at 700 °C and (b) variation of log(ASR) with log($P_{O_2}$).

The value of $n = 0.25$, estimated in the present study, indicates charge transfer process (Eq. (15)) is the limiting step. Mauvy et al. have observed change in slop at $P_{O_2} \approx 0.01$ atm in $Nd_{1.95}NiO_{4+\delta}$ MIEC [24]. According to them the ASR variation in this material has been due to change in oxygen stoichiometry. They concluded, on the basis of Eqs. (13)–(15), that at low $P_{O_2}$ (<0.01 atm) the reaction rate-limiting step has been a molecular oxygen absorption process, and at high $P_{O_2}$, the charge-transfer process has been the limiting step. A number of workers have analyzed the behaviour of $P_{O_2}$ dependent ASR in MIECs based on Eqs. (13)–(15) [42–44].

## 4. Conclusions

The acetate pyrolysis of reagents using microwave oven followed by microwave sintering yields superfine crystalline $Nd_{1.8}Ce_{0.2}CuO_{4\pm\delta}$ solid solution. The sintering of sample at high temperature increased the crystallite size and sintered density, which in turn enhances the microhardness number. The reduction in the crystallite size increased the crystal lattice volume of $Nd_{1.8}Ce_{0.2}CuO_{4\pm\delta}$. A good interfacial contact between $Ce_{0.9}Gd_{0.1}O_2$ electrolyte and $Nd_{1.8}Ce_{0.2}CuO_{4\pm\delta}$ cathode forms to yield symmetric cells for electrochemical studies. The Gerischer impedance is observed in the low frequency response of mixed conductor. Modeling impedance data with a Gerischer implies a chemical–electrochemical–chemical-type reaction at mixed–electronic–ionic conducting cathode. The sintering temperature 900 °C during cathode preparation is optimized on the basis of least area-specific-resistance (ASR) = 1.19 Ω cm$^{-2}$.

## References

[1] V.V. Kharton, A.P. Viskup, A.V. Kovalesvsky, E.N. Naumovich, F.M.B. Marques, Solid State Ionics 143 (2001) 337–353.
[2] Y. Wang, H. Nie, S. Wang, T. Wen, U. Guth, V. Valshook, Mater. Lett. 60 (2006) 1174–1178.
[3] V.V. Kharton, A.A. Yaremchenko, A.L. Shaula, M.V. Patrekeev, E.N. Naumovich, D.I. Logvinovich, J.R. Frade, F.M.B. Marques, J. Solid State Chem. 177 (2004) 26–37.
[4] A. Aguadero, J.A. Alonso, M.J. Escudero, L. Daza, Solid State Ionics 179 (11–12) (2008) 393–400.
[5] X. Dong, Z. Wu, X. Chang, W. Jin, N. Xu, Ind. Eng. Chem. Res. 46 (2007) 6910–6915.
[6] X. Ding, X. Kong, J. Jiang, C. Cui, J. Hydrogen Energy 34 (2009) 6869–6875.
[7] A. Aguadero, J.A. Alonso, M.T. Fernandez, M.J. Escudero, L. Daza, J. Power Sources 169 (2007) 17–21.
[8] J. Wan, J.B. Goodenough, J.H. Zhu, Solid State Ionics 178 (2007) 281–286.
[9] M.J. Escudero, A. Aguadero, J.A. Alonso, L. Daza, J. Electroanal. Chem. 611 (2007) 107–116.
[10] M.A. Daraukh, V.V. Vashook, H. Ullmann, F. Tietz, I. Arual Raj, Solid State Ionics 158 (2003) 141–150.
[11] V.V. Kharton, A.A. Yaremchenko, E.N. Naumovich, J. Solid State Electrochem. 3 (1999) 303–326.
[12] S.F. Palguev, V.K. Gilderman, V.I. Zemstov, High Temperature Oxide Electronic Conductors for Electrochemical Devices, Nauka, Moscow, 1990.
[13] M. Soorie, S.J. Skinner, Solid State Ionics 177 (2006) 2081–2086.
[14] A. Khandale, S.S. Bhoga, Solid State Ionics 182 (2011) 82–90.
[15] T.J.B. Holland, S.A.T. Redfern, Miner. Mag. 61 (1997) 65–77.
[16] K.R. Nagde, S.S. Bhoga, Ionics 16 (2010) 361–370.
[17] R.M. Belardi, J. Deseure, B. Caldeira, T. Matencio, R.Z. Domingues, Ionics 15 (2009) 227–232.
[18] G. Spinolo, M. Scavini, P. Ghigna, G. Chiodelli, G. Flor, Physica C 254 (1995) 359–369.
[19] E. Boehm, J.M. Bassat, M.C. Steil, P. Dordor, F. Mauvy, J.C. Grenier, Solid State Sci. 5 (2003) 973–981.
[20] J.B. Goodenough, A. Manthiram, J. Solid State Chem. 88 (1990) 115–139.
[21] F. Mauvy, J.M. Bassat, E. Boehm, P. Dordor, J.P. Loup, Solid State Ionics 158 (2003) 395–407.
[22] H. Takagi, S. Uchida, Y. Tokura, Phys. Rev. Lett. 62 (1989) 1197–1199.
[23] K. Singh, S.A. Acharya, S.S. Bhoga, Ionics 12 (2006) 295–301.
[24] F. Mauvy, C. Lalanne, J.M. Bassat, J.C. Grenier, H. Zhao, L. Huo, P. Stevens, J. Electrochem. Soc. 153 (8) (2006) A1547–A1553.
[25] A.B. Boukamp, H.J.M. Bouwmeester, Solid State Ionics 157 (2003) 29–33.
[26] D.R. Franceschetti, J.R. Macdonald, J. Electrochem. Soc. 138 (1991) 1368–1371.
[27] R.L. Hurt, J.R. Macdonald, Solid State Ionics 20 (1986) 111–124.
[28] D.R. Franceschetti, J.R. Macdonald, J. Electroanal. Chem. 100 (1979) 583–605.

[29] A.K. Jonscher, Dielectric Relaxation in Solids, Chelsea Dielectric Press, London, 1983.
[30] M. Gevers, Trans. Farad. Soc. 42A (1946) 47–55.
[31] J.R. Macdonald, M.K. Brachman, Rev. Mod. Phys. 28 (1956) 393–422.
[32] W. van Weperen, B.P.M. Lenting, E.J. Bijvank, H.W. den Hartog, Phys. Rev. B 16 (1977) 2953–2958.
[33] D. Ravaine, J.L. Souquet, Phys. Chem. Glasses 18 (1971) 27–31.
[34] I.D. Raistric, C. Ho, R.A. Huggins, J. Electrochem. Soc. 123 (1976) 1469–1476.
[35] A. Roos, D.R. Franceschetti, Solid State Ionics 12 (1984) 485–491.
[36] S.S. Bhoga, K. Singh, J. Phys. D: Appl. Phys. 33 (2000) 80–87.
[37] R.C. Makkus, K. Hemmes, J.H. de Wit, Ber. Bunsenges. Phys. Chem. 94 (1990) 960–967.
[38] R.U. Atangulov, I.V. Murygin, Solid State Ionics 67 (1993) 9–15.
[39] S. Adler, Solid State Ionics 111 (1998) 125–134.
[40] I.D. Raistrick, D.R. Franceschetti, J. Ross Macdonald, in: E. Barsoukov, J.R. Macdonald (Eds.), Impedance Spectroscopy, John Wiley & Sons, Inc., New Jersey, 2005, p. 13.
[41] E. Siebert, A. Hammouche, M. Kleitz, Electrochim. Acta 40 (1995) 1741–1753.
[42] F. Mauvy, J.M. Bassat, E. Boehm, J.P. Manaud, P. Dordor, J.C. Grenier, Solid State Ionics 158 (2003) 17–28.
[43] Q. Li, Y. Fan, H. Zhao, L.P. Sun, L.H. Huo, J. Power Sources 167 (2007) 64–68.
[44] L.P. Sun, Q. Li, H. Zhao, L.H. Huo, J.C. Grenier, J. Power Sources 183 (2008) 43–48.